AIAA JOURNAL
Vol. 44, No. 7, July 2006

Demonstration of Nonlinear Frequency Domain Methods

Matthew McMullen,* Antony Jameson,† and Juan Alonso‡
Stanford University, Stanford, California 94305 USA

DOI: 10.2514/1.15127

This paper demonstrates the accuracy of the nonlinear frequency domain method in applications to unsteady flow calculations. The basis of the method is a pseudospectral approach to recast a nonlinear unsteady system of equations in the temporal domain into a stationary system in the frequency domain. The nonlinear frequency domain method, in principle, provides the rapid convergence of a spectral method with increasing numbers of modes, and, in this sense, it is an optimal scheme for time-periodic problems. In practice it can also be effectively used as a reduced order method in which users deliberately choose not to resolve temporal modes in the solution. A variable-time-period method has been proposed such that the nonlinear frequency domain method can be applied to problems where the time period of the unsteadiness is either known or unknown a priori. To validate the latter case, results from this method have been compared with experimental results of vortex shedding in low Reynolds number flows past cylinders. Validation of the first case utilizes experimental data of a pitching airfoil in transonic flow. These comparisons demonstrate the efficiency of the nonlinear frequency domain method in representing complex nonlinear flow field physics with a limited number of temporal modes.

Nomenclature

A, B, C, D	=	coefficients used in the Strouhal data curve fit
b	=	component of the control volume face velocity vector
C_l	=	coefficient of lift
C_m	=	coefficient of moment
E	=	stagnation energy
F	=	component of flux vector contained in spatial operator
$\hat{I}$	=	Fourier coefficient of unsteady residual
k	=	wave number
L_α	=	lift transfer function
n	=	integer wave number
p	=	pressure
R	=	spatial residual
R_e	=	Reynolds number
S	=	cell face normal
S_t	=	Strouhal number
T	=	time period of the unsteady solution or temperature
t	=	time
u	=	component of the fluid velocity vector
V	=	volume
W	=	solution
x	=	spatial dimension
y^+	=	nondimensionalized distance from wall
γ	=	ratio of specific heats
δ_{ij}	=	Kronecker delta
κ	=	heat transfer coefficient
μ	=	absolute viscosity
ρ	=	density
σ	=	shear stress tensor
τ	=	pseudotime

Received 16 December 2004; revision received 8 August 2005; accepted for publication 13 September 2005.

*Department of Aeronautics and Astronautics. Member AIAA.
†Thomas V. Jones Professor of Engineering. Fellow AIAA.
‡Associate Professor of Engineering.

Introduction

THE calculation of unsteady flows continues to present a severe challenge to computational fluid dynamics (CFD). While preserving the accurate spatial discretizations associated with established steady-state solvers, unsteady codes also need to accurately resolve the time history of the solution. The challenge to CFD lies in this added dimension and its associated computational cost.

Unsteady flows can be divided into two main categories. The first category includes flows where the resolution of the initial transients is relevant, and accurate initial conditions are required. The second category includes flows where the user only requires the solution at a periodic steady state. As in the case of a steady flow simulation, the final periodic state is independent of the initial conditions.

The motivation of this research is to improve solver technologies for the second class of problems. There exist many physical problems within this class where boundary conditions force the unsteadiness at predetermined frequencies. Examples of this include the internal flows in turbomachinery, the external flow fields of helicopter blades or propellers, and certain aeroelastic computations. In contrast, the unsteadiness may also be induced by instability waves within the flow field. The resulting periodic flow is the result of boundary conditions, but the unsteadiness is not forced at any predetermined frequency. Examples in this group include (but are obviously not limited to) vortex shedding behind a cylinder and other fluid dynamic cases involving separated flows and free shear layers. Estimates of the frequencies of the unsteadiness can be gained via experimental data or simplified analytic models. However, the exact temporal frequencies for a given spatial discretization are usually impossible to determine a priori. The research presented in this paper focuses on methods that are amenable to both situations.

Several numerical approaches have been used to solve for unsteady periodic flows. Predominantly, time advancement schemes are applied to accurately resolve the flow transients until their decay to a periodic steady state. The efficiency of the technique is a function of the time scale of the transients relative to the time period of the converged oscillations. This approach can easily include all the flow field nonlinearities, but as these time scales diverge the cost of a time accurate calculation may become untenable. Linearizations can be applied to allow users to directly solve for the solution at its periodic steady state. The governing equations are linearized by splitting the solution into a steady and a significantly smaller periodic unsteady component. The cost of the procedure grows linearly with each mode

that can be solved independently of other modes. The approach gains numerical efficiency at the expense of limiting its applicability to flows where nonlinearities are insignificant.

Adamczyk [1] partially addressed this issue by proposing several different linearizations and averaging operators of the velocity variable to form what he termed the *deterministic* stress. Adamczyk proposed modeling these terms, but subsequent authors [2,3] proposed calculating these terms with a modified version of a linearized frequency domain solver, where the modes are coupled and require simultaneous solution of both the time-averaged and unsteady terms. Although some of the nonlinearities are addressed in the time-averaged solution, the higher order terms are still neglected in the solution of the unsteady modes. In addition, the method couples only the time-averaged solution to the higher harmonics. These shortcomings were remedied by Hall et al. [4] who proposed the harmonic balance technique to directly solve a fully coupled nonlinear system of equations at their periodic steady state. This research proposes the nonlinear frequency domain (NLFD) method which employs a similar pseudospectral approach but deviates from Hall's approach to improve the numerical efficiency of the algorithm.

Methodology

Governing Equations

For an arbitrary volume of fluid Ω, conservation of mass, momentum, and energy can be expressed in the following integral form:

$$\frac{d}{dt}\int_{\Omega} W dV + \oint_{\partial\Omega} \boldsymbol{F}\cdot\boldsymbol{N} ds = 0 \tag{1}$$

This integral form contains volumetric integrals denoted as $\int_{\Omega} dV$ and surface integrals denoted as $\oint_{\partial\Omega} ds$. For a two-dimensional flow, the physical properties of the fluid (density ρ, Cartesian velocity components u_i, and stagnation energy E) are collected into the state vector

$$W = \begin{bmatrix} \rho \\ \rho u_1 \\ \rho u_2 \\ \rho E \end{bmatrix} \tag{2}$$

The transport and/or production of these properties is accounted for in the flux vector $\boldsymbol{F}$. For convenience this overall flux is split into convective, $\boldsymbol{F}_c$, and viscous, $\boldsymbol{F}_v$, components

$$\boldsymbol{F} = \boldsymbol{F}_c - \boldsymbol{F}_v \tag{3}$$

The convective fluxes will include those terms normally associated with the Euler equations and the fluxes associated with a moving control volume. The velocity of the surface of the control volume is denoted as $\boldsymbol{b}$. Using indicial notation these terms can be defined for each coordinate direction i in two-dimensional space as

$$F_{c_i} = \begin{bmatrix} \rho & (u_i - b_i) & \\ \rho u_1 & (u_i - b_i) & +\delta_{1i}p \\ \rho u2 & (u_i - b_i) & +\delta_{2i}p \\ \rho E & (u_i - b_i) & +\delta_i p \end{bmatrix} \tag{4}$$

The viscous fluxes will include the stress tensor terms associated with viscous dissipation

$$F_{v_i} = \begin{bmatrix} 0 \\ \sigma_{i1} \\ \sigma_{i2} \\ u_j\sigma_{ij} + q_i \end{bmatrix} \tag{5}$$

Closure for the energy and viscous stress tensor terms is provided by the following relationships:

$$\begin{aligned} p &= (\gamma-1)\rho\left[E - \frac{1}{2}(u_j u_j)\right] \\ \sigma_{ij} &= \mu\left(\frac{\partial u_i}{\partial x_j} + \frac{\partial u_j}{\partial x_i}\right) + \lambda\delta_{ij}\frac{\partial u_k}{\partial x_k} \\ q_i &= \kappa\frac{\partial T}{\partial x_i} = \frac{\gamma}{\gamma-1}\frac{\mu}{P_r}\frac{\partial}{\partial x_i}\left(\frac{p}{\rho}\right) \end{aligned} \tag{6}$$

For all the analysis presented in this paper the ratio of specific heats γ and the Prandtl number P_r are held constant at 1.4 and 0.72, respectively. The relationship between absolute viscosity μ and temperature T is determined by Sutherland's law.

Transforming the Equations into the Frequency Domain

These equations are approximated using the finite volume approach where the continuous surface integrals are represented by a discrete summation of fluxes across a finite number of faces on the control volume. The remaining term in the conservation laws is the temporal derivative of the volumetric integral of the solution. This is approximated as the product of the cell volume with the temporal derivative of the average of the solution over the cell. The approximation of the flux vector $\boldsymbol{F}_c$ that ensures numerical stability is the subject of shock capturing theory, and is not the focus of this research. Any artificial dissipation provided by shock capturing schemes and/or turbulence modeling is denoted F_d while natural viscous dissipation is included in the $\boldsymbol{F}_v$ term.

$$V\frac{\partial W}{\partial t} + \sum_{cv}\boldsymbol{F}_c\cdot\boldsymbol{S} - \sum_{cv}F_d - \sum_{cv}\boldsymbol{F}_v\boldsymbol{S} = 0 \tag{7}$$

Note that Eq. (7) and all subsequent formulas derived from it are valid only for rigid mesh translation where the volume of each cell is not a function of time. The spatial operator R is introduced as a function of space and time including all the convective and dissipative fluxes. Taking advantage of this simplified notation, a semidiscrete form of the governing equations can be written as

$$V\frac{\partial W}{\partial t} + R = 0 \tag{8}$$

Assuming that the solution W and spatial operator R are periodic in time then both can be represented by separate Fourier series:

$$W = \sum_{k=-N/2}^{N/2-1}\hat{W}_k e^{ikt}, \qquad R = \sum_{k=-N/2}^{N/2-1}\hat{R}_k e^{ikt} \tag{9}$$

where,

$$i = \sqrt{-1} \tag{10}$$

These discrete Fourier transforms can be substituted into the semidiscrete form of the governing equations provided by Eq. (8), and the time derivative of the state variable can be moved inside the series summation. Taking advantage of the orthogonality of the Fourier terms results in a separate equation for each wave number k in the solution

$$ikV\hat{W}_k + \hat{R}_k = 0 \tag{11}$$

Here, however, each coefficient $\hat{R}_k$ of the transform of the residual depends on all the coefficients $\hat{W}_k$, because $R[W(t)]$ is a nonlinear function of $W(t)$. Thus (11) represents a nonlinear set of equations which must be iteratively solved. The solver attempts to find a solution W that drives this system of equations to zero for all wave numbers, but at any iteration in the solution process the unsteady

residual $\hat{I}_k$ will be finite:

$$\hat{I}_k = ikV\hat{W}_k + \hat{R}_k \tag{12}$$

The nonlinearity of the unsteady residual stems from the spatial operator. There are two approaches to calculating the spatial operator expressed in the frequency domain. The first uses a complex series of convolution sums to calculate $\hat{R}_k$ directly from $\hat{W}_k$. Such an approach was discussed in Hall's introductory paper on harmonic balance techniques [5]. Hall justly discarded the approach due to its massive complexity (considering artificial dissipation schemes and turbulence modeling) and cost that scales quadratically with the number of modes N.

An alternative proposed by Hall is to use the pseudospectral approach in the temporal domain. Our research employs a similar approach in the frequency domain. The advantage to this latter approach is in the application of the convergence acceleration techniques used in the NLFD code. Other research performed by this author demonstrates that the convergence rates of the unsteady residual in the NLFD solver are equivalent to steady-state codes [6]. In this approach, an unsteady residual exists for each wave number used in the solution and a pseudotime derivative acts as a gradient to drive the absolute value of all of these components to zero simultaneously.

$$V\frac{\partial \hat{W}_k}{\partial \tau} + \hat{I}_k = 0 \tag{13}$$

A diagram detailing the transformations used by the pseudospectral approach is provided in Fig. 1. We begin by assuming that $\hat{W}_k$ is known for all wave numbers. Using an inverse fast-Fourier-transform (FFT), $\hat{W}_k$ can be transformed back to the physical space resulting in a state vector $W(t)$ sampled at evenly distributed intervals over the time period. At each of these time instances the steady-state operator $R[W(t)]$ can be computed. A FFT is then used to transform the spatial operator to the frequency domain where $\hat{R}_k$ is known for all wave numbers. The unsteady residual $\hat{I}_k$ can then be calculated by adding $\hat{R}_k$ to the spectral representation of the temporal derivative $ikV\hat{W}_k$.

The cost of the FFT is proportional to $N\ \ell_n(N)$. For most realistic values of N ($N = 1 \rightarrow 10$) the cost of the pseudospectral approach is dominated by the cost associated with calculating the spatial operator. Consequently, the overall cost of the simulation scales by the product of the cost of evaluating a steady-state spatial operator and the number of time instances used to represent the solution N.

Boundary Conditions

Two separate sets of boundary conditions were employed for the model problems shown in subsequent sections. For the cylinder, a boundary condition based on the one-dimensional characteristic equations was implemented to provide a radiation free condition that essentially nullified any incoming waves. For the pitching airfoil, a steady Riemann invariant boundary condition was seperately applied to each time sample in the solution. These relatively simple boundary conditions take advantage of the diffusive character of the far-field grid. The degree to which these boundary conditions reflect energy is no longer a critical parameter given the de facto sponge created by grid diffusion and the extended distance of the boundary. If one used a time domain solver, the penalty associated with this approach would be the additional computational time required to propagate the unsteady waves across a larger domain. However, this is not the case for a frequency domain approach that solves directly for the solution at its periodic steady state.

Variable Time Period

A major outcome of our research has been the development of a gradient approach for the class of problems where the time period of the unsteadiness is unknown a priori. An iterative approach is proposed that determines the time period of the fundamental harmonic. In practice, the user provides an initial guess in the vicinity of the final answer and gradient information is used to change the estimate to the time period after each iteration in the solution process. Convergence is achieved when changes in the fundamental time period and all of the residual levels in the unsteady equations are negligible.

A derivation of the gradient-based-variable-time-period (GBVTP) method begins by noting that the wave number k is calculated by normalizing the sinusoidal period of oscillation 2π with the time period of interest T

$$k = \frac{2\pi n}{T} \tag{14}$$

The unsteady residual in Eq. (13) can then be written as a function of the time period T

$$\hat{I}_n = \frac{i2\pi nV}{T}\hat{W}_n + \hat{R}_n \tag{15}$$

The process of finding a solution to the unsteady flow equations is regarded as an optimization problem where the magnitude of the unsteady residual is minimized. A gradient of this residual with respect to the time period can be calculated and used to iteratively modify this time period until the magnitude of all components of the unsteady residual are negligible.

Because the unsteady residual $\hat{I}_n$ is a complex quantity, its magnitude squared is the sum of the square of its components. Using the chain rule, a gradient of this cost function with respect to the time period can be written as

$$\frac{1}{2}\frac{\partial |\hat{I}_n|^2}{\partial T} = \hat{I}_{nr}\frac{\partial \hat{I}_{nr}}{\partial T} + \hat{I}_{ni}\frac{\partial \hat{I}_{ni}}{\partial T} \tag{16}$$

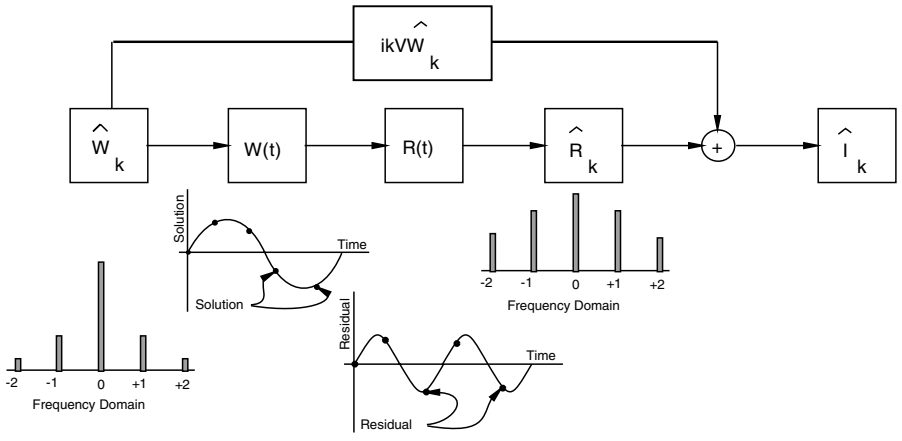

Fig. 1 Dataflow diagram of pseudospectral approach used to calculate spatial operator.

The quantity $\hat{I}_n$ is already calculated while monitoring the convergence of the solution (note that the real and imaginary parts of $\hat{I}_n$ are $\hat{I}_{nr}$ and $\hat{I}_{ni}$, respectively). The partial derivative terms can be expanded as

$$\frac{\partial \hat{I}_{nr}}{\partial T} = \frac{2\pi n V \hat{W}_{ni}}{T^2}, \qquad \frac{\partial \hat{I}_{ni}}{\partial T} = -\frac{2\pi n V \hat{W}_{nr}}{T^2} \tag{17}$$

The formulas can be further simplified by introducing cross product notation with the Fourier coefficients of the solution and residual written as vectors

$$\boldsymbol{W}_n = \hat{W}_{nr}\mathbf{e_1} + \hat{W}_{ni}\mathbf{e_2}, \qquad \boldsymbol{I}_n = \hat{I}_{nr}\mathbf{e_1} + \hat{I}_{ni}\mathbf{e_2} \tag{18}$$

Using this notation the gradient can be expressed as the magnitude of the cross product of the above vectors

$$\frac{1}{2}\frac{\partial |\hat{I}_n|^2}{\partial T} = \frac{2\pi n V}{T^2}|\boldsymbol{I}_n \times \boldsymbol{W}_n| \tag{19}$$

The time period can be updated using the gradient information by selecting a stable step ΔT

$$T^{n+1} = T^n - \Delta T \frac{\partial |\hat{I}_n|^2}{\partial T} \tag{20}$$

Typically one can start with an initial guess for the time period in the vicinity of the final answer. An unsteady flow solution can be obtained by solving the equations of motion at some nonzero residual level. The above gradient can then be used to adjust the time period at each iteration in the solution process. As such, both the solution and time period are simultaneously updated while the residual is driven to a negligible value.

To validate the GBVTP method, the NLFD code was used to calculate the flow over a cylinder (see section) at a Reynolds number of 105 in both fixed and variable-time-period modes. First, a variable-time-period case was executed where the NLFD code obtained a solution for the field variables and time period associated with a machine-zero residual. Then a number of fixed-time-period calculations were performed using time periods in the vicinity of the one derived by the GBVTP case. In Fig. 2, the minimum residual obtained by each of these fixed-time-period runs is plotted as a function of the distance between the constant time period and that determined by the GBVTP method. The plot shows that to obtain machine-zero level residuals using fixed-time-period calculations the Strouhal number specified by the user a priori must approximate the GBVTP value to machine accuracy. The results from this numerical experiment demonstrate the capability of the GBVTP algorithm to find this value. In addition, since there is only one minimum in the residual values, the data support the notion that there is a unique Strouhal number associated with the exact solution of the discretized equations.

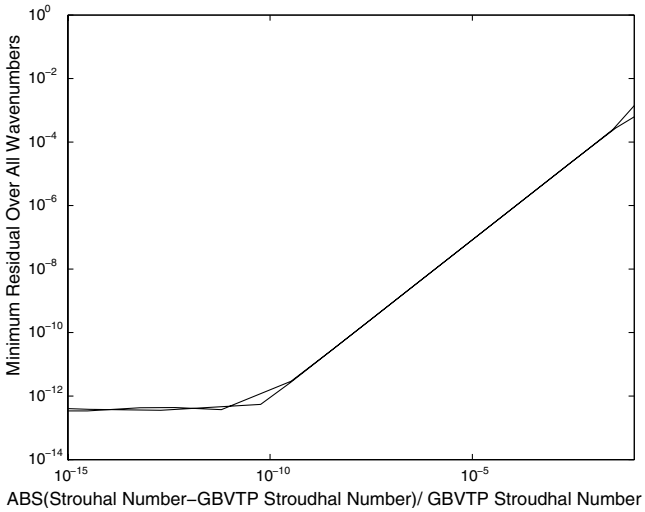

Fig. 2 Minimum residual of a fixed-time-period NLFD calculation.

Cylindrical Vortex Shedding

Test Case Description

This section will compare results from the NLFD code with results obtained from independently conducted experiments of laminar vortex shedding behind a cylinder. Given the work of Williamson in this field [7,8], his experimental data will be used exclusively for these comparisons. In addition, comparisons are also made with Henderson's [9] numerical results that employ spectral elements with an eighth order basis.

Cylinder Results

Both spatial and temporal resolution surveys were conducted as part of this research. The spatial surveys utilized four independently generated grids, while the temporal surveys used a varying number of wave numbers in the representation of the solution. For each permutation of spatial and temporal resolution, we calculated 10 cylinder solutions at different Reynolds numbers between 60 and 150. Table 1 identifies all values of the three different parameters used in these surveys. Including all the permutations, 160 different solutions were calculated.

Variable-Time-Period Results

Figure 3 provides the Strouhal frequency statistics as a function of Reynolds number for each temporal resolution computed on the finest grid. For comparative purposes, Williamson's [7,10,11] experimental data is overplotted on the graphs with circles.

The difference between the experimental data and the one mode solution actually increases with increasing Reynold number. This variation can be explained by computing the L^2 norm of the energy within the solution for each harmonic:

$$\|E_k\| = \left[\int_\Omega |\hat{\rho} e_k|^2 dV\right]^{1/2} \tag{21}$$

Figure 4 plots this norm as a function of the Reynolds number for the finest grid used in the spatial survey. This plot shows that the relative energy in the higher harmonics increases as the Reynolds number increases. At the upper end of the Reynolds number range, the unresolved modes alias more energy back into the lower modes leading to a variation in the predicted Strouhal number between the 3 and 5-mode solutions. At the lower end of the Reynolds number range, the higher modes carry substantially less energy and fewer modes are required to accurately predict Strouhal number and other statistics.

For each numerical solution, the Strouhal and Reynolds numbers form a dependent pair that can be used to solve a least squares problem for the coefficients A, B, C (assuming $D = 0$) in Eq. (22).

$$S_t = A + \frac{B}{R_e + D} + C(R_e + D) \tag{22}$$

Table 1 Values of parameters used in the three-dimensional parametric survey, which combines both temporal and spatial resolution surveys over a range in Reynolds number.

Variable	Values
N Modes	1, 3, 5, 7
Grid	129×65, 193×81, 257×129, 385×161
Reynolds number	60, 70, 80, 90, 100, 110, 120, 130, 140, 150

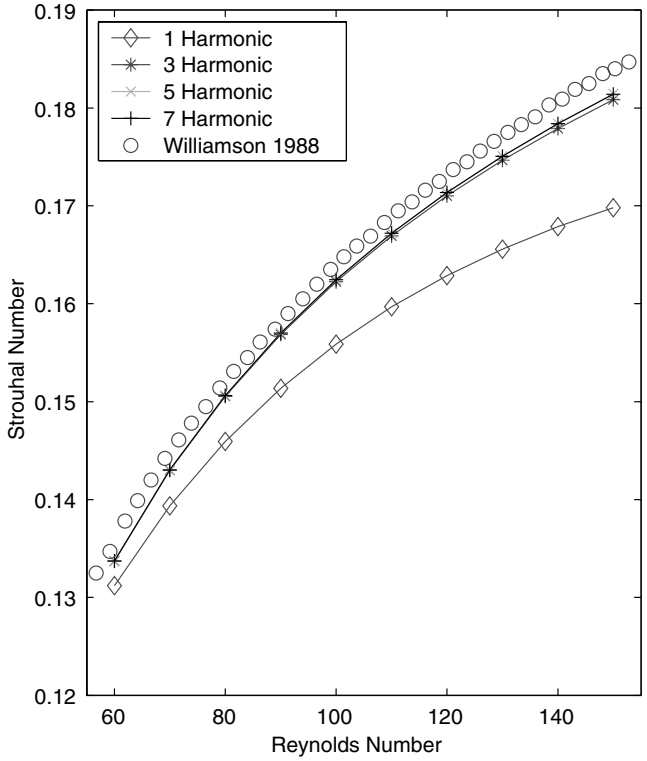

Fig. 3 Strouhal number as a function of Reynolds number.

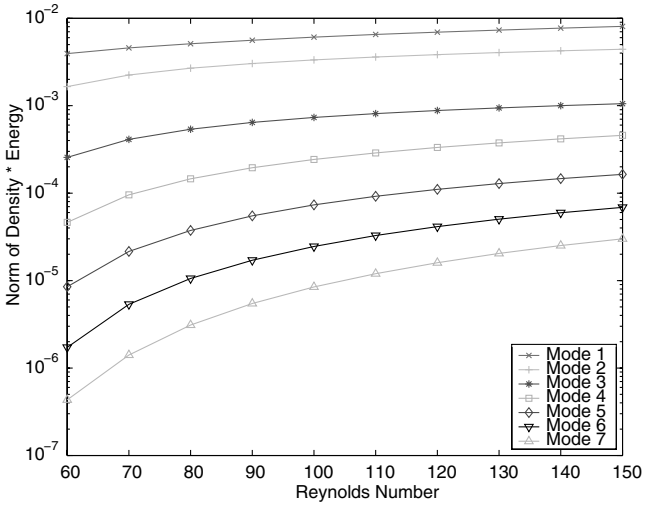

Fig. 4 Norm of the energy as a function of Reynolds number.

The shift operator D, can then be chosen such that the error between the curve fit equation (using the coefficients A, B, C derived from the numerical data) and the experimental results is minimized. This parameter represents a statistically averaged Reynolds number shift between the experimental and numerical datasets, and is provided in Table 2.

Because of the limited number of converged solutions, the data for the coarsest mesh are suspect and have not been included. In general, the Reynolds number shift decreases by a factor of 4 for every doubling in the grid size. This error component has a dissipative influence lowering the effective Reynolds number of the numerical solution. Notably, the magnitude of the shift operator is temporally converged after using just three time varying harmonics.

Table 2 Shift in Reynolds number between the NLFD calculations and the experimental dataset for all permutations of temporal and spatial resolution.

N Modes	193 × 81 Grid	257 × 129 Grid	385 × 161 Grid
1	44.7	31.1	19.3
3	33.5	8.7	3.3
5	33.6	8.5	2.9
7	33.6	8.6	2.9

Fixed-Time-Period Results

This section explores the relative merits of the GBVTP algorithm by comparing a flow field statistic based on solutions computed with and without the GBVTP algorithm. Figure 5 plots the base suction coefficient (the negative mean pressure coefficient at the far leeward edge of the cylinder) as a function of Reynolds number, for both fixed-time-period and GBVTP data sets. The fixed-time-period results used a constant time period based on interpolation of the experimental data.

In most cases, the GBVTP algorithm effectively moves the numerical results closer to the experimental data; representing a positive influence on the accuracy of the NLFD method. This effect is most noticeable for the coarse grid results shown in subplot (a) of Fig. 5. This can be explained using Table 2 showing that differences in Strouhal numbers between NLFD and experimental data increase with decreasing spatial resolution. This inverse relationship implies according to Fig. 2 that the minimum residual obtained for coarse grid calculations will be much greater than that associated with the fine grid. Ultimately, these larger residuals manifest themselves as an increased error in the base suction coefficient predicted on the coarse grid and provide an explanation as to why the effects of the GBVTP algorithm vary with spatial resolution.

As with the Strouhal number results, the difference between the NLFD and experimentally predicted base suction coefficient results decreases with decreasing Reynolds number. Again this can most likely be attributed to the varying levels of aliasing error with Reynolds number documented by Fig. 4. Surprisingly, this difference between NLFD and experimental results on the finest mesh is smaller than the difference between the Henderson results and the experimental data over the entire range in Reynolds numbers.

Pitching Airfoil Experimental Validation

This section compares the numerical results produced by the NLFD code with results obtained from independently conducted experiments of a pitching airfoil rotating periodically about its quarter chord at a given frequency. Far-field quantities such as angle of attack, velocity, and thermodynamic properties of the fluid are held constant in time. The convergence of these results is assessed by surveys of spatial and temporal resolution based on global force coefficients. The experimental data used for comparison was compiled by Davis [12] and published in Agard report 702. This section uses the dataset identified by the experimentalist as the priority case within the report (Dataset 2, CT Case 6, Dynamic Index 55).

A C-mesh grid topology has been used exclusively for the Navier–Stokes calculations of the pitching airfoil. The grids were generated with the a hyperbolic mesh generation tool. The average height of the first cell adjacent to the wall is quantified in Table 3 in terms of y^+ units based on a Reynolds number of 12.5×10^6 for the 64A010 airfoil. Other descriptive parameters including grid dimensions and far-field boundary distances are also provided in Table 3.

Coefficient of Lift Results

Figures 6 provides C_l predictions as a function of temporal resolution for the finest grid. To facilitate comparison, the experimental results are overplotted for all the cases. Most importantly, the results exhibit little variation over the range of temporal resolutions; one time varying mode provides a solution convergent to plotting accuracy.

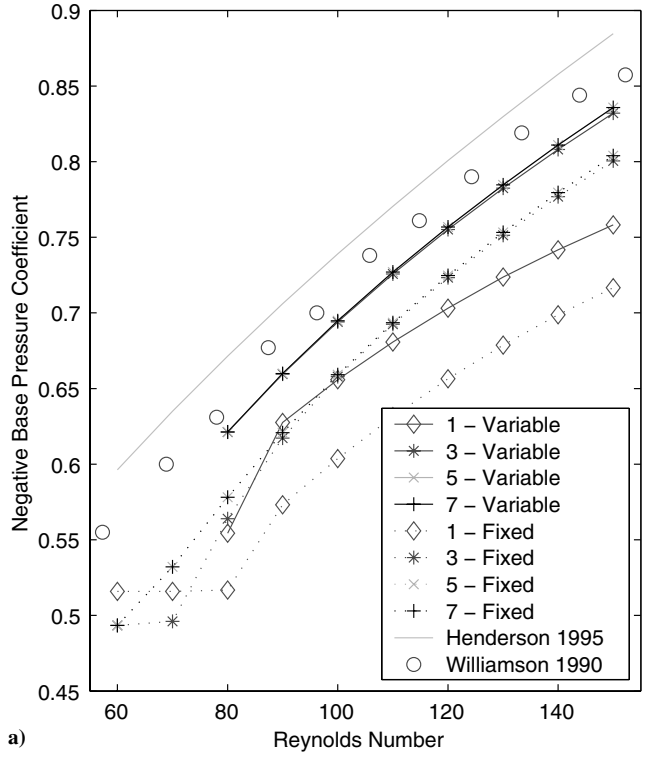

a)

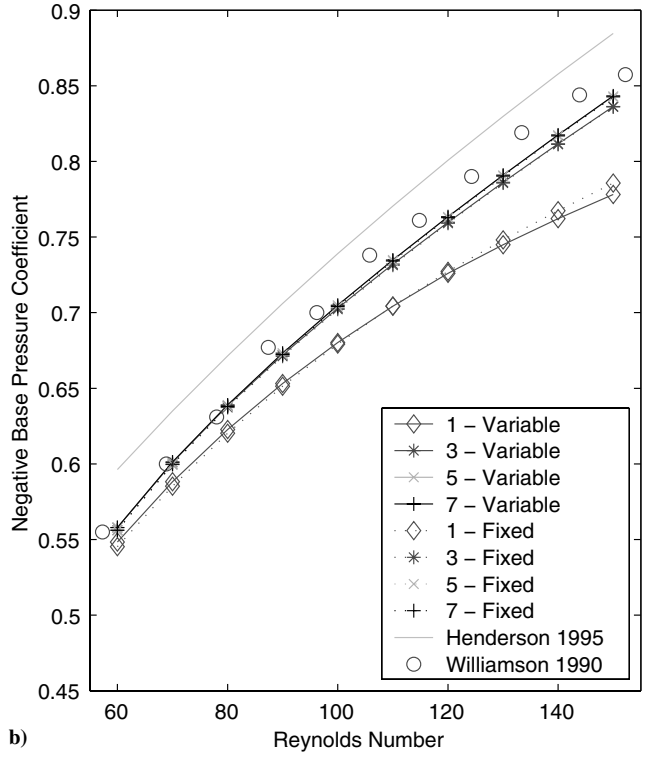

b)

Fig. 5 Base suction coefficient as a function of Reynolds number. a) 193 × 81 grid; b) 385 × 161 grid.

Transfer functions are introduced to quantify the time varying results presented in the previous paragraph. The magnitude of this transfer function is computed by dividing the magnitude of the Fourier coefficient for C_l at a given wave number by the magnitude of the Fourier coefficient for α at the same wave number

Table 3 Description of meshes employed for the NLFD Navier–Stokes calculations.

Dimensions	Boundary distance (chords)	Distance from first cell to wall (y^+)
129 × 33	15	11.6
193 × 49	12	6.9
257 × 65	12	3.8

Table 4 Magnitude ($\|\hat{C}_{l_1}\|/\|\hat{\alpha}_1\|$) and phase shift ($\angle\hat{C}_{l_1} - \angle\hat{\alpha}_1$) lift transfer functions for various spatial and temporal resolutions.

Source	1 Mode	2 Mode	3 Mode
	Magnitude		
Experiment		0.095	
129 × 33	0.104	0.103	0.103
193 × 49	0.097	0.097	0.097
257 × 65	0.101	0.101	0.101
	Phase shift		
Experiment		−25.6	
129 × 33	−20.3	−20.0	−20.1
193 × 49	−20.9	−20.9	−20.9
257 × 65	−20.0	−20.0	−20.0

$$L_\alpha = \frac{\hat{C}_{l_k}}{\hat{\alpha}_k} = \frac{\|\hat{C}_{l_k}\|}{\|\hat{\alpha}_k\|} e^{i(\angle\hat{C}_{l_k} - \angle\hat{\alpha}_k)} \tag{23}$$

This is analogous to the lift curve slope commonly used in the analysis of steady-state airfoils. The phase lag of the transfer function is defined as the difference in phase angles between the Fourier coefficients for C_l and α quantified in terms of degrees. The phase angle represents the fraction of the time period that the coefficient of lift lags behind the angle of attack.

Table 4 provides the magnitudes and phase lags of the lift transfer for the fundamental harmonic. The deviation between the NLFD and experimental results is on average 5.5% for the magnitude of the lift transfer function and 20.3% (5.2°) for the phase shift. No distinct trends are found in the data as spatial resolution is varied, and little variation is exhibited as a function of temporal resolution. These statistics reconfirm the results presented in Fig. 6; in that adding time varying modes into the solution provides no significant improvement.

Coefficient of Moment Results

Figure 7 provides C_m predictions as a function of temporal resolution. The experimental results are overplotted for all the cases to facilitate the comparison with the numerical results.

The numerical results show little variation as a function of temporal resolution. In all cases, the variation between the turbulent Navier–Stokes calculations and experimental results is still significant. Although not documented here, numerical experiments have been performed [6] that show time accurate techniques (based on a 3-4-1 implicit discretization of the temporal derivative) and NLFD methods converging to identical answers as temporal resolution increases. Since time accurate solvers and NLFD methods converge to the same answer the disagreement between the C_m data results should not be attributable to the method used in discretizing the temporal derivative. Rather, the source of this discrepancy can be found in other aspects of the numerics (boundary conditions and/or spatial discretization including turbulence modeling) or in the experimental data.

We can provide bounds as to the magnitude of the latter case by investigating post-test corrections applied to raw data gathered in modern experiments. Green et al. [13,14] have provided such data for a 0012 airfoil tested in NASA's Transonic Cryogenic Tunnel using both slotted and adaptive wall technologies. For angles of attack whose magnitude were less than 2° over a variety of runs, the post-test Wall Interference Assessment/Correction code provided mean

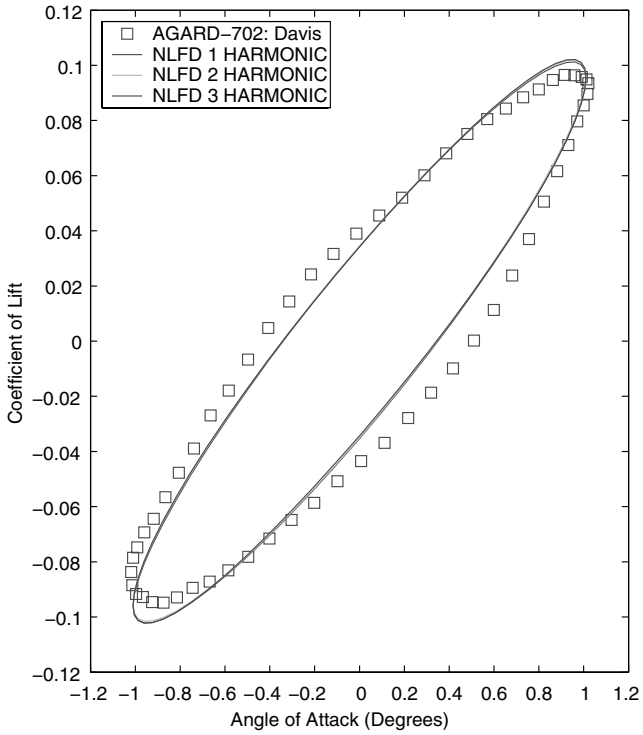

Fig. 6 Lift coefficients as a function of the instantaneous angle of attack provided from unsteady Navier–Stokes NLFD calculations and Davis's 64A010 experiment.

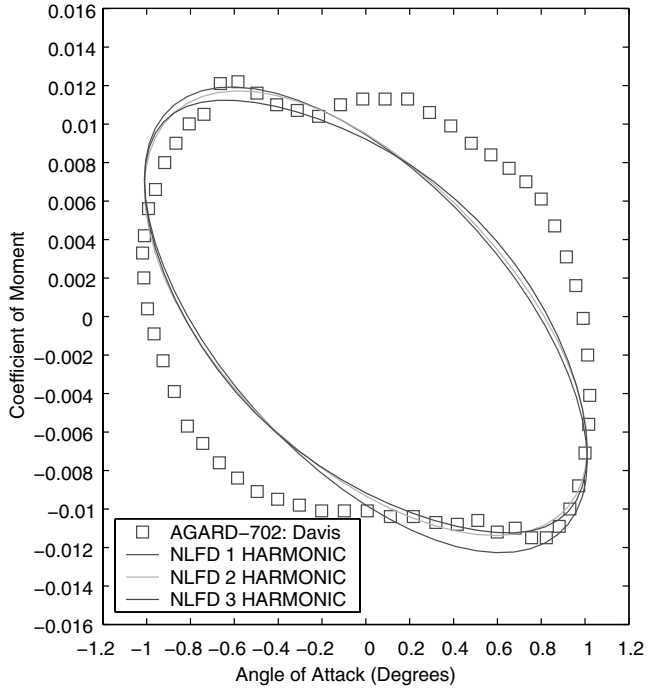

Fig. 7 Moment coefficients as a function of the instantaneous angle of attack provided from unsteady Navier–Stokes NLFD calculations and Davis's 64A010 experiment.

C_m corrections of 6.25×10^{-4} and mean angle of attack corrections of 0.33°. Given differences between experiments, these steady results should not be directly compared with corrections that could be made for unsteady experiments. However, these observations in conjunction with the temporal convergence experiments referenced in the previous paragraph, seem to suggest that more research needs to be performed on the spatial operators. Unfortunately, little conclusive evidence is offered in regard to the variation in C_m results as a function of spatial resolution. There is some variation in the results between the different meshes, but no consistent trend is observed between grid refinement and improving the agreement with experimental results.

Conclusions

For the cylindrical vortex shedding problem, the temporal resolution survey shows that only three time varying modes are required to predict the Strouhal number and base suction coefficient to engineering accuracy for the entire range of laminar Reynolds numbers. However, the energy in the higher harmonics decreases with decreasing Reynolds number. At the lower end of the Reynolds number range, one or two modes can be used to achieve results that are as accurate as three mode calculations at the higher end of the range. Surprisingly, some of the NLFD results are closer to the experimental data than the Henderson results calculated using a very high order method.

Using an initial guess based on experimental data, the GBVTP method can be used to predict the time period of the fundamental harmonic. This shedding frequency is unique for a given discretization and boundary conditions, and is the only frequency that will allow the unsteady residual to decay to zero. In general, the GBVTP method improved the agreement between the numerical and experimental results for base suction coefficient in comparison to methods where the time-period was fixed a priori. The improvement is largely a function of the difference between the shedding frequency value associated with the fixed-time-period calculation and the final value predicted by the GBVTP method.

The motivation for selecting the transonic pitching airfoil model problem was to demonstrate the ability of the NLFD method to accurately resolve flows of engineering importance in turbulent viscous environments. The numerical experiments confirm the accuracy and efficiency of the NLFD method for this problem. It is remarkable that using just one time varying mode, the NLFD predictions for coefficient of lift provide excellent agreement with experimental results. Numerical tests confirm that NLFD is an order of magnitude more efficient than dual time stepping methods for periodic unsteady flows of the type presented here.

References

[1] Adamczyk, J. J., "Model Equation for Simulating Flows in Multistage Turbomachinery," NASA TM-86869, November 1984.

[2] Chen, T., Vasanthakumar, P., and He, L., "Analysis of Unsteady Blade Row Interaction Using Nonlinear Harmonic Approach," *Journal of Propulsion and Power*, Vol. 17, No. 3, 2001, pp. 651–658.

[3] He, L., and Ning, W., "Nonlinear Harmonic Analysis of Unsteady Transonic Inviscid and Viscous Flows," in *Unsteady Aerodynamics and Aeroelasticity of Turbomachines: Proceedings of the 8th International Symposium, Stockholm, Sweden, 1997*, edited by T. H. Fransson, Kluwer Academic, Dordrecht, Boston, 1998.

[4] Hall, K. C., "Seminar on Harmonic Balance Techniques, January 2000," presented to the Aerospace Computing Lab, Stanford University.

[5] Hall, K. C., Thomas, J. P., and Clark, W. S., "Computation of Unsteady Nonlinear Flows in Cascades Using a Harmonic Balance Technique," Technical Rept., *Proceedings of the 9th International Symposium on Unsteady Aerodynamics, Aeroacoustics and Aeroelasticity of Turbomachines (ISUAAAT) and Legendre Lecture Series, Lyon, France, 2000*, edited by P. Ferrand and S. Aubert, Presses Universitaires de Grenoble, 2000.

[6] McMullen, M. S., "The Application of Non-Linear Frequency Domain Methods to the Euler and Navier–Stokes Methods," Ph.D. Dissertation, Stanford University, 2003.

[7] Williamson, C. H. K., "Defining a Universal and Continuous Strouhal–Reynolds Number Relationship for the Laminar Vortex Shedding of a Circular Cylinder," *Physics of Fluids*, Vol. 31, No. 10, 1988, p. 2742.

[8] Williamson, C. H. K., "Vortex Dynamics in the Cylinder Wake," *Annual Review of Fluid Mechanics*, Vol. 28, 1996, pp. 477–539.

[9] Henderson, R. D., "Details of the Drag Curve near the Onset of Vortex Shedding," *Physics of Fluids*, Vol. 7, No. 9, 1995.
[10] Williamson, C. H. K., "The Existence of Two Stages in the Transition to Three- Dimensionality of a Cylinder Wake," *Physics of Fluids*, Vol. 31, No. 11, 1988, p. 3165.
[11] Williamson, C. H. K., "Three-Dimensional Wake Transition," *Journal of Fluid Mechanics*, Vol. 328, Dec. 1996, pp. 345–407.
[12] Davis, S. S., "NACA 64A010 (NASA Ames Model) Oscillatory Pitching," AGARD, Rept. 702, January 1982, Dataset 2.
[13] Green, L., Zhang, Q., Garriz, J., Wang, S., Vatsa, V., Haigler, K., and Newman, P., "NASA/CAE Wind Tunnel Interference Cooperative Program—Status and Sample Results, ICAW, Paper W1, 1991.
[14] Green, L. L., and Newman, P. A., "Wall-Interfence Assessment and Corrections for Transonic NACA 0012 Airfoil Data from Various Wind Tunnels," NASA Technical Paper 3070, April 1991.

D. Gaitonde
Associate Editor